Nonparaxial vector-field modeling of optical coherence tomography and interferometric synthetic aperture microscopy

Brynmor J. Davis,* Simon C. Schlachter, Daniel L. Marks, Tyler S. Ralston, Stephen A. Boppart, and P. Scott Carney

Department of Electrical and Computer Engineering, Beckman Institute for Advanced Science and Technology,
University of Illinois at Urbana–Champaign, 405 North Mathews Street, Urbana, Illinois 61801, USA
*Corresponding author: bryn@uiuc.edu

A large-aperture, electromagnetic model for coherent microscopy is presented and the inverse scattering problem is solved. Approximations to the model are developed for near-focus and far-from-focus operations. These approximations result in an image-reconstruction algorithm consistent with interferometric synthetic aperture microscopy (ISAM): this validates ISAM processing of optical-coherence-tomography and optical-coherence-microscopy data in a vectorial setting. Numerical simulations confirm that diffraction-limited resolution can be achieved outside the focal plane and that depth of focus is limited only by measurement noise and/or detector dynamic range. Furthermore, the model presented is suitable for the quantitative study of polarimetric coherent microscopy systems operating within the first Born approximation. © 2007 Optical Society of America

OCIS codes: 100.3190, 100.6890, 170.1650, 170.4500, 110.6880, 180.3170.

1. INTRODUCTION

Traditionally in optical microscopy there has been a perceived trade-off between depth of focus and resolution; i.e., one cannot be improved without adversely affecting the other. Hence, techniques that use high-numerical-aperture (NA) focusing, such as confocal microscopy [1], optical coherence microscopy (OCM) [2], and multiphoton microscopy [3], are restricted to generating *en face* images unless the sample is translated axially or optical mechanisms are used to scan the focus. Techniques that produce cross-sectional images without axial translation of the focus, such as optical coherence tomography (OCT) [4], use low-NA focusing so that a pencil beam approximation can be used. Nevertheless, transverse resolution degrades away from the focus in these techniques.

It has been shown in a recent series of papers [5–9] that this spatially varying resolution can be corrected in interferometric optical microscopy, overcoming the trade-off between depth of focus and resolution, by using a computational technique known as interferometric synthetic aperture microscopy (ISAM). The coherent nature of the ISAM imaging modality permits the solution of an inverse problem in order to provide a volumetric reconstruction of the object based only on a planar scanning geometry. ISAM uses a quantitative scattering model and a simple inversion technique to reconstruct the object with spatially invariant resolution. The superior imaging performance of ISAM is realized through an improved understanding of the physical relationship connecting the detected signal and the object imaged, a relationship not fully exploited in classical OCT.

Interferometric microscopies collect data that are dependent on both the phase and amplitude of the field scattered from the object of interest. This represents a major advantage over incoherent techniques, such as wide-field or confocal microscopy, where the phase of the field is lost. Coherent detection allows the complex amplitude of the field, rather than just intensity, to be measured or inferred. In broadband interferometric instruments such as OCT and ISAM, data are collected over a range of wavelengths, in addition to two spatial dimensions, to obtain a three-dimensional volume of data. This in turn allows the inference of three-dimensional object structure. In OCT image reconstruction, it is implicitly assumed that at each planar scan position a simple Fourier-transform relation exists between the frequency dependence of the measured field and the depth dependence of the imaged object. In contrast, ISAM reconstruction takes into account the multiplex relation between the data and the object structure. Inverting this relation allows a spatially invariant diffraction-limited image resolution to be achieved, in contrast to OCT where this resolution is achieved only at the focal plane. The spatially invariant ISAM resolution should be expected, as the only difference in the field (as opposed to the intensity) scattered from different *en face* planes can be understood as a change in the complex weighting of the plane-wave components of the angular spectrum of the field. The ability to computationally manipulate these weightings, as allowed by interferometric measurement, means that any *en face* plane can be brought into focus computationally after data are collected. The computational focusing implemented in ISAM is analogous to that used in synthetic aperture radar [10] (SAR), which is also a broadband, coherent technique.

Previous developments of ISAM were based on a scalar model of Gaussian-beam focusing and scattering. This is a simplification, as light is a vector wave and Gaussian op-

tics satisfy Maxwell's equations only when the paraxial approximation is invoked. A full vectorial model is developed to describe the effects of polarization on scattering and propagation and also to account for high-angle fields. In addition, no particular beam apodization is required by the new model, meaning that various imaging modalities that may not use a Gaussian beam can also be accommodated in this new framework. Resulting analysis and numerical experiments provide a verification of the approximate scalar model previously used to justify ISAM processing. The ISAM method is shown to also be applicable in the case of a tightly focused (high-NA) beam. Furthermore, a means to reconcile paraxial (low-NA) [5] and high-NA [6] limits is presented. Thus the new model adds rigor to the theoretical framework of ISAM and also extends its realm of applicability.

The vector-based forward model is constructed using the standard model for high-NA, vectorial focusing [11] of the illumination field. Scattering from the object is then modeled using the first Born approximation, and the resulting field is propagated back through a lens to the detector. It is shown that this model can be approximated in a manner consistent with previous ISAM results. Simulations confirm that the ISAM Fourier-resampling procedure can still be expected to give excellent results in a vectorial and/or high-angle framework. High-angle lenses are shown to give the expected increase in resolution but without any loss of depth of focus or signal level away from the focal plane.

2. FORWARD MODEL

In this section the physics of the imaging system are modeled. A general coherent microscope is considered, but one particular configuration can be seen in Fig. 1. In this section, interferometric microscopy is briefly discussed before the model is constructed. The construction proceeds by first considering a focused illumination field, then the response of the sample, followed by focused detection of the scattered light. The consequences of using the same lens for illumination and detection are also considered.

A. Interferometric Microscopy

OCT, which is a form of interferometric microscopy, measures the three-dimensional structure of a sample by scattering broadband radiation from it. As shown in Fig. 1 a focused beam of broadband light is scanned through a sample, and the interferometric cross correlation between the scattered signal and a reference signal is recorded at a photodetector. By sampling the interferometric cross correlation at many wavenumbers k, and by translating the focus of the beam to many positions $\mathbf{r}^{(o)}$ within the sample, the three-dimensional structure of the sample can be estimated.

For spectral-domain OCT [12,13], the detected intensity $I(\mathbf{r}^{(o)};k)$ for focal point $\mathbf{r}^{(o)}$ and wavenumber k is

$$I(\mathbf{r}^{(o)};k) = |\mathbf{E}^{(r)}(k) + \mathbf{E}^{(s)}(\mathbf{r}^{(o)};k)|^2 = |\mathbf{E}^{(r)}(k)|^2 + |\mathbf{E}^{(s)}(\mathbf{r}^{(o)};k)|^2$$

$$+ 2\,\mathrm{Re}\{[\mathbf{E}^{(r)}(k)]^H\mathbf{E}^{(s)}(\mathbf{r}^{(o)};k)\}, \qquad (1)$$

where $\mathbf{E}^{(r)}(k)$ is the reference field, $\mathbf{E}^{(s)}(\mathbf{r}^{(o)};k)$ is the scattered field at the detector, and superscript H indicates the
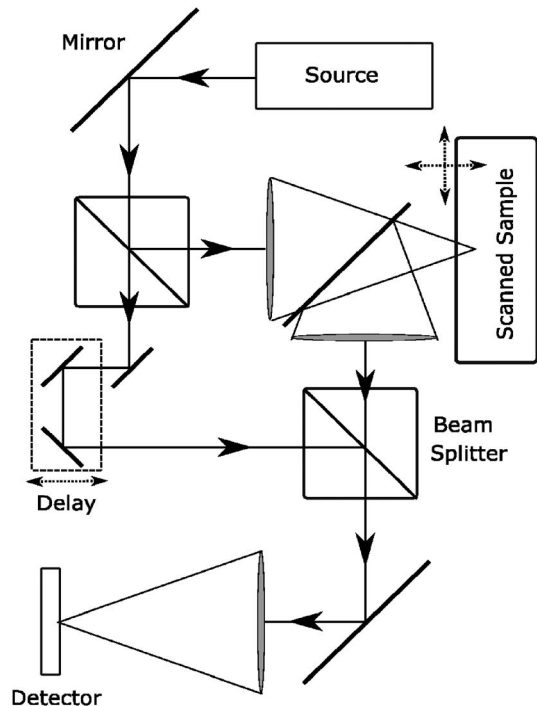

Fig. 1. Basic illustration of a coherent microscope. A source feeds an interferometer where one arm produces a reference field and the other consists of illumination and detection from the sample to be imaged. The reference arm may contain an adjustable delay element (represented here by movable mirrors). In practical implementations, the Mach–Zehnder layout shown here is often replaced by a Michelson interferometer using a single objective lens. The sample is scanned mechanically or optically in two or three dimensions.

Hermitian conjugation operator. A term can be identified with the interferometric cross correlation, which is denoted by

$$S(\mathbf{r}^{(o)};k) = [\mathbf{E}^{(r)}(k)]^H\mathbf{E}^{(s)}(\mathbf{r}^{(o)};k). \qquad (2)$$

Assuming the autocorrelation term $|\mathbf{E}^{(s)}(\mathbf{r}^{(o)};k)|^2$ is negligible, measurements of $I(\mathbf{r}^{(o)};k)$ for one or more known reference fields $\mathbf{E}^{(r)}(k)$ allow the cross-correlation $S(\mathbf{r}^{(o)};k)$ to be inferred. The effects of nonnegligible autocorrelation terms in ISAM imagery have been investigated in a separate publication [14]. Because a single measurement of $I(\mathbf{r}^{(o)};k)$ can determine only $\mathrm{Re}\{S(\mathbf{r}^{(o)};k)\}$, the phase of the reference may be varied by $\pi/2$ to also measure $\mathrm{Im}\{S(\mathbf{r}^{(o)};k)\}$ using phase-shifting interferometry [15,16].

The cross-correlation signal $S(\mathbf{r}^{(o)};k)$ can be related to the signal measured using time-domain OCT. Given that $k(\omega)$ is the dispersion relation of the sample medium, relating temporal frequency ω to spatial frequency k, the temporal cross-correlation signal as a function of delay τ is

$$S_T(\mathbf{r}^{(o)};\tau) = \frac{1}{2\pi}\int_{-\infty}^{\infty} S(\mathbf{r}^{(o)};k(\omega))e^{i\omega\tau}\mathrm{d}\omega. \qquad (3)$$

By utilizing a procedure to correct the material dispersion [17], the signal $S(\mathbf{r}^{(o)};k)$ can be estimated from $S_T(\mathbf{r}^{(o)};\tau)$, with a resampling coordinate change from ω to k. In practice, however, typically only $\mathrm{Re}\{S_T(\mathbf{r}^{(o)};\tau)\}$ is measured using time-domain OCT. The effect of this is that only the

real part of the sample susceptibility can be reconstructed.

Likewise, in the practice of spectral-domain OCT, it is often inconvenient to perform phase shifting to recover the imaginary part of $S(\mathbf{r}^{(o)},k)$ so that only $\mathrm{Re}\{S(\mathbf{r}^{(o)},k)\}$ is measured. If the signal $S(\mathbf{r}^{(o)},k)$ corresponds to a time-domain signal $S_T(\mathbf{r}^{(o)},\tau)$ such that $S_T(\mathbf{r}^{(o)};\tau)=0$ for $\tau<0$, then the real part and the imaginary part of $S(\mathbf{r}^{(o)},k)$ are related through a Hilbert transform over k [18]. This condition can be ensured by combining the reference and sample signals such that the reference signal completely precedes the sample signal in time. The Hilbert transformation can be implemented in practice using the Fourier transform, followed by nulling of all negative frequency components. Such a procedure provides a method of measuring the full complex $S(\mathbf{r}^{(o)},k)$ without using multiple measurements.

B. Focused Illumination

An objective lens is assumed to be illuminated by plane waves of amplitude $\mathbf{E}^{(i)}P(k)$ traveling parallel to the optic axis (the case of non-plane-wave illumination is easily modeled by including the illumination pattern in the lens model, as demonstrated in Subsection 3.E). Here $\mathbf{E}^{(i)}$ is a unit vector and $P(k)$ is proportional to the temporal Fourier transform of the illumination field, or in the case of incoherent illumination, the square root of the power spectral density. It is also assumed that the objective lens is infinity corrected—i.e., it is designed to focus an incoming plane wave to the focal point. This geometry is most conveniently analyzed by considering the illuminating field on a planar surface across the instrument side of the objective lens, while the field immediately after the lens will be represented on a spherical reference surface centered on the focal point. Thus the instrument-side pupil is planar, while the object-side pupil is spherical and centered around the focal point. The field produced on the object side of the lens may be described by a spectrum of plane waves [11], $\mathbf{E}^{(l)}(\sigma_x,\sigma_y)$, which is given by the expression

$$\mathbf{E}^{(l)}(\sigma_x,\sigma_y) = \bar{\mathbf{A}}(\sigma_x,\sigma_y)\mathbf{E}^{(i)}P(k). \qquad (4)$$

Here σ_x and σ_y define the propagation direction of a member of the plane-wave spectrum. Specifically, they are the sines of the angles between the propagation direction and the optic axis of the lens. The action of the lens on the input plane wave is given by the dyad $\bar{\mathbf{A}}(\sigma_x,\sigma_y)$, and since this expression does not depend on the wavenumber k, the lens is implicitly assumed to be achromatic. Chromatic aberrations could be included by taking a k-dependent dyad. Note that $\bar{\mathbf{A}}(\sigma_x,\sigma_y)$ has been defined as a function of the angle to focus, rather than the lateral position on the object-side pupil, but the mapping between the two is straightforward: $\sigma_x=-(x-x^{(o)})/\zeta$, $\sigma_y=-(y-y^{(o)})/\zeta$, where ζ is the focal length and the three-tuple $\mathbf{r}^{(o)}=(x^{(o)},y^{(o)},z^{(o)})$ gives the location of the geometric focus. The elements σ_x,σ_y define a unit vector $\boldsymbol{\sigma}=[\sigma_x,\ \sigma_y,\ \sigma_z(\sigma_x,\sigma_y)]$, where

$$\sigma_z(\sigma_x,\sigma_y) = +\sqrt{1-\sigma_x^2-\sigma_y^2}. \qquad (5)$$

This vector points from each location on the object-side pupil to the focus. Positive z points from the lens toward the focal region.

Expressions describing the lens $\bar{\mathbf{A}}(\sigma_x,\sigma_y)$ are well known; e.g., for an aplanatic lens $\bar{\mathbf{A}}(\sigma_x,\sigma_y)$ may be obtained by simple rotations of the expression given by Eq. (2.23) in [11]. Modifications can be made to model pupil-plane filters, aberrations, or more complicated effects such as the spatially varying polarization used in radially polarized beams. The field on the object-side pupil [given in Eq. (4)] determines the field in the vicinity of the focal point [19]. The field produced by a unit-amplitude incident wave will be denoted by $\mathbf{g}(\mathbf{r}-\mathbf{r}^{(o)};k)$ with its focus at $\mathbf{r}^{(o)}$:

$$\mathbf{g}(\mathbf{r}-\mathbf{r}^{(o)};k) = -\frac{ik}{2\pi}\int_\Omega \frac{\bar{\mathbf{A}}(\sigma_x,\sigma_y)\mathbf{E}^{(i)}}{\sigma_z(\sigma_x,\sigma_y)}e^{ik\boldsymbol{\sigma}\cdot(\mathbf{r}-\mathbf{r}^{(o)})}\mathrm{d}\sigma_x\mathrm{d}\sigma_y. \qquad (6)$$

Here evanescent waves do not contribute to the focused field, so Ω is the region in (σ_x,σ_y) space for which $\sigma_z(\sigma_x,\sigma_y)$ is real—i.e., the unit disk, $\Omega=\{\sigma_x,\sigma_y:\sigma_x^2+\sigma_y^2<1\}$. The effective region of integration will actually be smaller than Ω due to the limited angular extent of the aperture; however, this effect will be modeled by setting $\bar{\mathbf{A}}(\sigma_x,\sigma_y)$ to zero outside the aperture.

The object describes all inhomogeneities except, perhaps, a single planar boundary between free space and a high-index background. To account for the background, the illumination amplitude described in Eq. (6) (and the entire model developed in this paper) can be adjusted by rescaling the spatial axes. The effects of the boundary between free space and the imbedding medium can be captured by defining a virtual lens in the style of [20]. Using this method, the effects of the boundary will be included in the lens models.

C. Scattering from the Object

The field $P(k)\mathbf{g}(\mathbf{r}-\mathbf{r}^{(o)})$ interacts with the object and, under the first Born approximation, produces a secondary source of density $-k^2P(k)\bar{\boldsymbol{\eta}}(\mathbf{r})\mathbf{g}(\mathbf{r}-\mathbf{r}^{(o)};k)$, where $\bar{\boldsymbol{\eta}}(\mathbf{r})$ is the susceptibility of the object. The field produced by scattering from the object is treated perturbatively within the accuracy of the first Born approximation. It is important to recognize that higher-order terms in the Born series for the scattered field will introduce signal originating from apparently greater depth and will effectively be noise in the signal. This is also the case in standard OCT, where multiple scattering will produce artifacts and limit the overall depth of penetration for which the method is effective.

The tensor susceptibility $\bar{\boldsymbol{\eta}}(\mathbf{r})$ may be anisotropic but is assumed to be constant with k. The secondary source can now be propagated through space using the Green's tensor $\bar{\mathcal{G}}(\mathbf{r}',\mathbf{r};k)$. This tensor takes a source at $\mathbf{r}$ to a field at $\mathbf{r}'$. For an illumination focal point of $\mathbf{r}^{(o)}$, the unfocused scattered field at a position $\mathbf{r}'$ can be calculated as

$$\mathbf{E}^{(u)}(\mathbf{r}',\mathbf{r}^{(o)};k) = -k^2 P(k) \int \bar{\mathcal{G}}(\mathbf{r}',\mathbf{r};k)\bar{\boldsymbol{\eta}}(\mathbf{r})\mathbf{g}(\mathbf{r}-\mathbf{r}^{(o)};k)\mathrm{d}^3 r.$$

$$(7)$$

The Green's tensor can also be expressed in an angular spectrum using the vectorial Weyl's identity [21,22]. The spectrum will be limited to propagating waves, as evanescent waves will not contribute at the observation position, so that

$$\bar{\mathcal{G}}(\mathbf{r}',\mathbf{r};k) = \frac{ik}{2\pi}\int_\Omega \frac{\bar{\mathbf{D}}(\sigma_x,\sigma_y)}{\sigma_z(\sigma_x,\sigma_y)}e^{\pm ik\boldsymbol{\sigma}\cdot(\mathbf{r}'-\mathbf{r})}\mathrm{d}\sigma_x\mathrm{d}\sigma_y, \qquad z' \gtrless z.$$

$$(8)$$

Here $\bar{\mathbf{D}}(\sigma_x,\sigma_y)$ is a dyad that ensures only valid polarization states, i.e., those that are transverse to the direction of propagation, are included. It will be assumed that the observation point is on the lens side of the source so that $z' < z$. The above spectral representation can now be used in Eq. (7):

$$\mathbf{E}^{(u)}(\mathbf{r}',\mathbf{r}^{(o)};k)$$

$$= -k^2 P(k) \int \frac{ik}{2\pi}\int_\Omega \frac{\bar{\mathbf{D}}(\sigma_x,\sigma_y)}{\sigma_z(\sigma_x,\sigma_y)}$$

$$\times e^{ik\boldsymbol{\sigma}\cdot(\mathbf{r}-\mathbf{r}')}\mathrm{d}\sigma_x\mathrm{d}\sigma_y \bar{\boldsymbol{\eta}}(\mathbf{r})\mathbf{g}(\mathbf{r}-\mathbf{r}^{(o)};k)\mathrm{d}^3 r$$

$$= -k^2 P(k) \int \frac{ik}{2\pi}\int_\Omega \frac{\bar{\mathbf{D}}(\sigma_x,\sigma_y)}{\sigma_z(\sigma_x,\sigma_y)}$$

$$\times e^{ik\boldsymbol{\sigma}\cdot(\mathbf{r}-\mathbf{r}^{(o)})}e^{-ik\boldsymbol{\sigma}\cdot(\mathbf{r}'-\mathbf{r}^{(o)})}\mathrm{d}\sigma_x\mathrm{d}\sigma_y \bar{\boldsymbol{\eta}}(\mathbf{r})\mathbf{g}(\mathbf{r}-\mathbf{r}^{(o)};k)\mathrm{d}^3 r.$$

$$(9)$$

The factor of $e^{-ik\boldsymbol{\sigma}\cdot\mathbf{r}^{(o)}}e^{ik\boldsymbol{\sigma}\cdot\mathbf{r}^{(o)}}=1$ has been inserted so that the field can be represented as an integral of a spectrum of plane waves of the form $e^{-ik\boldsymbol{\sigma}\cdot(\mathbf{r}'-\mathbf{r}^{(o)})}$. Each such plane wave is traveling back toward the lens in the $-\boldsymbol{\sigma}$ direction and has accumulated a phase corresponding to its distance from the focal point. Such a representation is convenient when considering detection optics focused to $\mathbf{r}^{(o)}$.

D. Focused Detection
The signal acquired results from collecting the scattered light with a lens. This collection operation is modeled using the backward-propagating angular spectrum of Eq. (9). It is assumed that the detection lens is also focused to $\mathbf{r}^{(o)}$. The tensor $\bar{\mathbf{B}}(\sigma_x,\sigma_y)$ defines the detection lens by mapping an object-side plane wave traveling in the $-\boldsymbol{\sigma}$ direction to the resulting plane-wave component that travels parallel to the optic axis on the instrument side of the lens. An integration is performed over the scattered plane waves, and the result is projected onto the reference field $\mathbf{E}^{(r)}(k)$ as in Eq. (2). The analysis presented here may encompass any reference field $\mathbf{E}^{(r)}(k)$ but, as indicated in Fig. 1, the reference field will generally have the same spectral content as the field illuminating the sample. As such, it will be represented by $\mu_r^* P(k)\mathbf{E}^{(d)}$, where μ_r controls the ratio of the reference- and illumination-field amplitudes, and $\mathbf{E}^{(d)}$ is the detected polarization (like $\mathbf{E}^{(i)}$,

$\mathbf{E}^{(d)}$ is a unit vector). Again, a limited aperture can be modeled by having $\bar{\mathbf{B}}(\sigma_x,\sigma_y)$ fall to zero outside the aperture. The collected signal is therefore expressed as follows:

$$S(\mathbf{r}^{(o)},k) = -k^2 \mu_r |P(k)|^2 (\mathbf{E}^{(d)})^H \int\int_\Omega \bar{\mathbf{B}}(\sigma_x,\sigma_y)\frac{ik}{2\pi}\frac{\bar{\mathbf{D}}(\sigma_x,\sigma_y)}{\sigma_z(\sigma_x,\sigma_y)}$$

$$\times e^{ik\boldsymbol{\sigma}\cdot\mathbf{r}^{(o)}}\mathrm{d}\sigma_x\mathrm{d}\sigma_y \bar{\boldsymbol{\eta}}(\mathbf{r})\mathbf{g}(\mathbf{r}-\mathbf{r}^{(o)};k)\mathrm{d}^3 r. \qquad (10)$$

Comparing this expression with Eq. (2), it can be seen that the reference field $\mathbf{E}^{(r)}(k)$ accounts for a factor of $\mu_r P^*(k)(\mathbf{E}^{(d)})^H$ and that the remainder of Eq. (10) describes the scattered field $\mathbf{E}^{(s)}(\mathbf{r}^{(o)};k)$.

Equation (10) can be simplified by noting that $\bar{\mathbf{D}}(\sigma_x,\sigma_y)$ is the identity operator for fields perpendicular to the direction of propagation and the null operator for fields parallel to it. Since the lens accepts only fields perpendicular to the incident ray path,

$$\bar{\mathbf{B}}(\sigma_x,\sigma_y)\bar{\mathbf{D}}(\sigma_x,\sigma_y) = \bar{\mathbf{B}}(\sigma_x,\sigma_y). \qquad (11)$$

This allows $\bar{\mathbf{D}}(\sigma_x,\sigma_y)$ to be removed from Eq. (10).
Analogously to the illumination pattern of Eq. (6), a detection pattern can be defined as

$$\mathbf{f}(\mathbf{r}-\mathbf{r}^{(o)};k) = -\frac{ik}{2\pi}\int_\Omega \frac{\bar{\mathbf{B}}^T(\sigma_x,\sigma_y)(\mathbf{E}^{(d)})^*}{\sigma_z(\sigma_x,\sigma_y)}e^{ik\boldsymbol{\sigma}\cdot(\mathbf{r}-\mathbf{r}^{(o)})}\mathrm{d}\sigma_x\mathrm{d}\sigma_y,$$

$$(12)$$

where superscript * represents conjugation and superscript T the transpose operation. This can be used to give a simple form to Eq. (10):

$$S(\mathbf{r}^{(o)},k) = k^2 \mu_r |P(k)|^2 \int \mathbf{f}^T(\mathbf{r}-\mathbf{r}^{(o)};k)\bar{\boldsymbol{\eta}}(\mathbf{r})\mathbf{g}(\mathbf{r}-\mathbf{r}^{(o)};k)\mathrm{d}^3 r$$

$$= k^2 \mu_r |P(k)|^2 \int f_\alpha(\mathbf{r}-\mathbf{r}^{(o)};k)g_\beta(\mathbf{r}-\mathbf{r}^{(o)};k)\eta_{\alpha\beta}(\mathbf{r})\mathrm{d}^3 r$$

$$= \int h_{\alpha\beta}(\mathbf{r}^{(o)}-\mathbf{r};k)\eta_{\alpha\beta}(\mathbf{r})\mathrm{d}^3 r. \qquad (13)$$

The last two lines employ Einstein summation notation and show how each component of the susceptibility affects the collected data. The function $h_{\alpha\beta}(\mathbf{r})$ is a point-spread function and is defined as

$$h_{\alpha\beta}(\mathbf{r};k) = \mu_r k^2 |P(k)|^2 f_\alpha(-\mathbf{r};k)g_\beta(-\mathbf{r};k). \qquad (14)$$

These equations represent the most general form of the forward model. In the following subsection, the case where the same lens is used for illumination and detection is explored. Note that the results given in this section can be generalized to cover partially polarized detection provided that the correlation between each component of $\mathbf{E}^{(d)}$ and $\mathbf{E}^{(i)}$ is known. For the sake of brevity, such an analysis will not be presented here. The model can also be used in an analysis of polarization-sensitive imaging by taking measurements with differing $\mathbf{E}^{(i)}$ and/or $\mathbf{E}^{(d)}$. However, it should be noted that anisotropies in the background medium are not accounted for in the model presented here.

E. Single-Lens Systems

Most practical systems will include only a single lens, and this will be used for both illumination and detection. This system is illustrated in Fig. 2. For a single-lens system the following relation applies:

$$\bar{\mathbf{B}}^T(\sigma_x, \sigma_y) = \bar{\mathbf{A}}(\sigma_x, \sigma_y). \tag{15}$$

This result stems from a simple application of optical reciprocity [23].

If the detection polarization is chosen to be the same as the illumination polarization, but propagating in the opposite direction, i.e., back out of the object, then the following relation must hold [23]:

$$\mathbf{E}^{(d)} = \left[\mathbf{E}^{(i)}\right]^*. \tag{16}$$

If the conditions of Eqs. (15) and (16) are met, then Eq. (12) becomes the same as Eq. (6), indicating that the illumination and detection patterns are the same—$\mathbf{f}(\mathbf{r} - \mathbf{r}^{(o)}; k) = \mathbf{g}(\mathbf{r} - \mathbf{r}^{(o)}; k)$. This results in the following model for the OCT system:

$$S(\mathbf{r}^{(o)}, k) = k^2 \mu_r |P(k)|^2 \int \mathbf{g}^T(\mathbf{r} - \mathbf{r}^{(o)}; k) \bar{\boldsymbol{\eta}}(\mathbf{r}) \mathbf{g}(\mathbf{r} - \mathbf{r}^{(o)}; k) \mathrm{d}^3 r. \tag{17}$$

This equation is analogous to Eq. (3.18) in [5] but is derived in a more general setting. Additionally, it can be seen that the detection operation is of the form

$$S(\mathbf{r}^{(o)}, k) = k^2 \mu_r |P(k)|^2 \int \mathbf{g}^T(\mathbf{r} - \mathbf{r}^{(o)}; k)[\cdot] \mathrm{d}^3 r. \tag{18}$$

For a fixed-energy secondary source, the detected signal is maximized when the secondary source is proportional to $\mathbf{g}^*(\mathbf{r} - \mathbf{r}^{(o)}; k)$. This corresponds to a counterpropagating version of the illumination field. As this field would be traveling back through the same lens that produced it, it would indeed be expected to maximize the expected signal. Conversely, if $\bar{\boldsymbol{\eta}}(\mathbf{r})$ is uniform, then the secondary
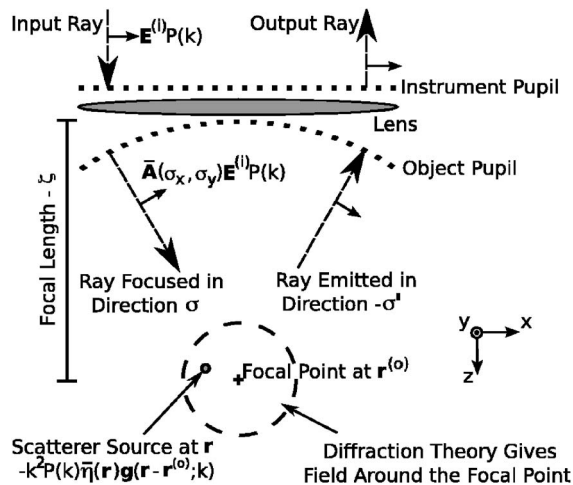

Fig. 2. Diagram illustrating a single-lens OCT system. Some of the expressions derived in Section 2 are shown with the physical quantities they represent. Following standard practice, a ray optics description characterizes the lens. This description can then be interpreted as an angular spectrum and be used to calculate the fields in the vicinity of the focal spot.

source field in Eq. (17) would be $\mathbf{g}(\mathbf{r} - \mathbf{r}^{(o)}; k)$ (i.e., without conjugation), and it can be shown that the detected signal would, as expected, be zero for this no-scatterer case.

F. Data Collection

The imaging system will produce a data set by obtaining $S(\mathbf{r}^{(o)}, k)$ at many values of $\mathbf{r}^{(o)}$. If this scanning is performed in all three dimensions, then Eq. (13) is a sum of the three-dimensional convolutions over the components of the tensor susceptibility. The inverse problem (reconstruction of the susceptibility from the data) could then be tackled in the Fourier domain, where the convolution operation becomes a simple multiplication.

However, it is desirable to have a fast imaging system that scans only in the two dimensions perpendicular to the optic axis (x and y)—the remaining dimension (z) can be reconstructed if spectral information is gathered. In the convention adopted here, the x and y directions will be called the lateral dimensions, and z points in the axial direction. The scanning offset $\mathbf{r}^{(o)}$ will be split into axial and lateral components

$$\mathbf{r}^{(o)} = (x^{(o)}, y^{(o)}, z^{(o)}) = (\mathbf{r}_\parallel^{(o)}, z^{(o)}). \tag{19}$$

The forward model given in Eq. (13) can be written as

$$S(\mathbf{r}_\parallel^{(o)}, k) = \int \int h_{\alpha\beta}(\mathbf{r}_\parallel^{(o)} - \mathbf{r}_\parallel, z^{(o)} - z; k) \eta_{\alpha\beta}(\mathbf{r}_\parallel, z) \mathrm{d}^2 r_\parallel \mathrm{d}z. \tag{20}$$

The inner integral in Eq. (20) is a convolution. Letting the symbols $\tilde{S}(\cdot)$, $\tilde{h}_{\alpha\beta}(\cdot)$ and $\tilde{\eta}_{\alpha\beta}(\cdot)$ denote the two-dimensional Fourier transforms over the lateral dimensions of $S(\cdot)$, $h_{\alpha\beta}(\cdot)$, and $\eta_{\alpha\beta}(\cdot)$, respectively, gives

$$\tilde{S}(\mathbf{Q}_\parallel, k) = \int \tilde{h}_{\alpha\beta}(\mathbf{Q}_\parallel, z^{(o)} - z; k) \tilde{\eta}_{\alpha\beta}(\mathbf{Q}_\parallel, z) \mathrm{d}z. \tag{21}$$

This is a sum (over α and β) of one-dimensional Fredholm integral equations of the first kind (FIEFK) at each lateral Fourier point. If each term in the sum of Eq. (21) can be isolated or the anisotropy of the object is known, inverting the FIEFK is a standard problem [24]. The kernel $\tilde{h}_{\alpha\beta}(\mathbf{Q}_\parallel, z^{(o)} - z; k)$ can be calculated from known theory [11], and this one-dimensional case should be computationally tractable. However, inverting the entire data set will require many such operations and so may be time-consuming. For this reason, a computationally efficient, approximate inversion process will be explored.

3. APPROXIMATE MODELS

A mathematical model for a coherent microscope with a planar scanning geometry and spectral detection, i.e., an OCT system, was described in the previous section. Although this model is complete, it may be possible to introduce simplifying approximations [5,6]. The goal is to simplify the form of the model—specifically, to take the FIEFK relation of Eq. (21) and reduce it to a simple resampling operation.

A. Alternate Representation of the Point-Spread Function

The point-spread function given by Eq. (14) is determined by the product $f_\alpha(\mathbf{r};k)g_\beta(\mathbf{r};k)$. These functions are naturally expressed in the Fourier domain; Eqs. (6) and (12) will be rewritten as

$$f_\alpha(\mathbf{r};k) = -\frac{ik}{2\pi}\int_\Omega \frac{F_\alpha(\sigma_x,\sigma_y)}{\sigma_z(\sigma_x,\sigma_y)}e^{ik\boldsymbol{\sigma}\cdot\mathbf{r}}d\sigma_x d\sigma_y, \qquad (22)$$

$$g_\beta(\mathbf{r};k) = -\frac{ik}{2\pi}\int_\Omega \frac{G_\beta(\sigma_x,\sigma_y)}{\sigma_z(\sigma_x,\sigma_y)}e^{ik\boldsymbol{\sigma}\cdot\mathbf{r}}d\sigma_x d\sigma_y, \qquad (23)$$

where

$$F_\alpha(\sigma_x,\sigma_y) = [\bar{\mathbf{B}}^T(\sigma_x,\sigma_y)(\mathbf{E}^{(d)})^*]_\alpha, \qquad (24)$$

$$G_\beta(\sigma_x,\sigma_y) = [\bar{\mathbf{A}}(\sigma_x,\sigma_y)\mathbf{E}^{(i)}]_\beta. \qquad (25)$$

The limits of integration of Eqs. (22) and (23) can be extended to infinity as the aperture pattern is zero outside Ω. Since these equations are then in the form of inverse Fourier transforms, it can be seen that

$$\tilde{f}_\alpha(\mathbf{Q}_\parallel,z;k) = -2\pi i\frac{F_\alpha\left(\dfrac{\mathbf{Q}_\parallel}{k}\right)}{k_z(\mathbf{Q}_\parallel)}e^{ik_z(\mathbf{Q}_\parallel)z}, \qquad (26)$$

$$\tilde{g}_\beta(\mathbf{Q}_\parallel,z;k) = -2\pi i\frac{G_\beta\left(\dfrac{\mathbf{Q}_\parallel}{k}\right)}{k_z(\mathbf{Q}_\parallel)}e^{ik_z(\mathbf{Q}_\parallel)z}, \qquad (27)$$

where $\mathbf{Q}_\parallel = k\boldsymbol{\sigma}_\parallel$ and $k_z(\mathbf{Q}_\parallel) = k\sigma_z(\mathbf{Q}_\parallel/k)$. Strictly speaking $\mathbf{Q}_\parallel$ and $k_z(\mathbf{Q}_\parallel)$ are functions of k, but this will not be noted explicitly.

To calculate $h_{\alpha\beta}(\mathbf{r};k)$ the product $f_\alpha(\mathbf{r};k)g_\beta(\mathbf{r};k)$ is relevant, as shown by Eq. (14):

$$\tilde{h}_{\alpha\beta}(-\mathbf{Q}_\parallel,-z;k) = k^2\mu_r|P(k)|^2[\tilde{f}_\alpha(\mathbf{Q}_\parallel,z;k)*_\parallel\tilde{g}_\beta(\mathbf{Q}_\parallel,z;k)]. \qquad (28)$$

This lateral convolution (denoted by $*_\parallel$) can be written explicitly as

$$\tilde{h}_{\alpha\beta}(-\mathbf{Q}_\parallel,-z;k) = -4\pi^2 k^2\mu_r|P(k)|^2$$
$$\times\int \frac{F_\alpha\left(\dfrac{\mathbf{q}_\parallel}{k}\right)G_\beta\left(\dfrac{\mathbf{Q}_\parallel-\mathbf{q}_\parallel}{k}\right)}{k_z(\mathbf{q}_\parallel)\,k_z(\mathbf{Q}_\parallel-\mathbf{q}_\parallel)}$$
$$\times e^{i[k_z(\mathbf{q}_\parallel)+k_z(\mathbf{Q}_\parallel-\mathbf{q}_\parallel)]z}d^2q_\parallel. \qquad (29)$$

The Fourier-domain representation of $\tilde{h}_{\alpha\beta}(-\mathbf{Q}_\parallel,-z;k)$ given in Eq. (29) will form the basis for approximation of the forward model. Two separate approximations will be derived—one for scatterers near focus and one for scatter-ers far from focus. It will be seen that the form of the resultant expression for the data is the same in both cases.

B. Approximation for Far-from-Focus Scatterers

Since $F_\alpha(\mathbf{q}_\parallel/k)$ and $G_\beta(\mathbf{q}_\parallel/k)$ have a fixed scale and the rate of complex oscillation in Eq. (29) increases with $|kz|$, there will be some distance from the focus at which the two-dimensional method of stationary phase [22] can be applied. The method of stationary phase can be applied to integrals whose integrand contains a rapidly oscillating complex exponential. The value of such integrals are determined by the value of the integrand at the stationary points of the argument of the exponential—that is, points where the argument of the exponential has zero gradient. In this problem that occurs at the point

$$\mathbf{q}_\parallel^{(\text{stat.})} = \mathbf{Q}_\parallel/2. \qquad (30)$$

The method of stationary phase then gives

$$\tilde{h}_{\alpha\beta}(-\mathbf{Q}_\parallel,-z;k) \approx \frac{i4\pi^3 k}{z}\mu_r|P(k)|^2 e^{i2k_z(\mathbf{Q}_\parallel/2)z}$$
$$\times F_\alpha\left(\frac{\mathbf{Q}_\parallel/2}{k}\right)G_\beta\left(\frac{\mathbf{Q}_\parallel/2}{k}\right). \qquad (31)$$

The accuracy of this approximation improves as the oscillations in the integrand become more rapid and as the domain of integration increases. These two conditions are quantified by $|kz|$ and NA^2, respectively. The parameter $NA^2|kz|$ will be chosen to determine the applicability of the approximation based on these quantities and on the fact that this parameter is proportional to the distance from the focus, in units of the Rayleigh range. The example analytical and numerical results given in Subsections 3.E and 5.C support the use of $NA^2|kz|$ in determining where the stationary phase approximation is applicable. It should be noted that the stationary phase approximation also relies on the aperture profiles $F_\alpha(\mathbf{q}_\parallel/k)$, $G_\beta(\mathbf{q}_\parallel/k)$ being smooth within the domain of integration. In the next section, the near-focus approximation will be seen to take a form similar to Eq. (31).

As shown in Eq. (31), for far-from-focus scatterers the $-\mathbf{Q}_\parallel$ component of the lateral-Fourier-domain data is dependent only on a single point $\mathbf{Q}_\parallel/(2k)$ in the apertures. This point can be associated with a ray path from the apertures to the focal point and shows that the far-from-focus interactions can be interpreted in a geometrical optics framework. The derivation presented in this subsection is analogous to standard derivations of geometrical optics from Maxwell's equations, as in [25], Chapter 3.

In the case that $\mathbf{Q}_\parallel/(2k)$ falls outside one or both of the apertures, there is no stationary point within the limits of the integral in Eq. (29). This is because the limits of the integral are determined by the regions of nonzero overlap between $F_\alpha(\mathbf{q}_\parallel/k)$ and $G_\beta((\mathbf{Q}_\parallel-\mathbf{q}_\parallel)/k)$. In such a case, the next order in the asymptotic series for $\tilde{h}(\cdot)$ is proportional to $|kz|^{-3/2}$ (the lowest-order term being proportional to $|kz|^{-1}$) and is associated with the point of stationary phase constrained to the boundary of the overlap of the apertures [22]. That contribution is usually called the bound-

ary ray and becomes the dominant term in the shadow of one aperture or the other [26].

C. Approximation for Near-Focus Scatterers

For small values of $|kz|$, i.e., when a scatterer is near the focal plane, the oscillations of the complex exponential in Eq. (29) will be slow. Therefore, for sufficiently small $|kz|$, the functions $F_\alpha(\mathbf{q}_\parallel/k)$ and $G_\beta(\mathbf{q}_\parallel/k)$ will be narrowly peaked with respect to the remainder of the integrand in Eq. (29). This peakedness allows the integral to be approximated.

Before proceeding with the approximation, it will be convenient to assume the standard case of aplanatic objective lenses. This means the pupil functions can be written as

$$F_\alpha(\sigma_x, \sigma_y) = \check{F}_\alpha(\sigma_x, \sigma_y)\sqrt{\sigma_z(\sigma_x, \sigma_y)}, \qquad (32)$$

$$G_\beta(\sigma_x, \sigma_y) = \check{G}_\beta(\sigma_x, \sigma_y)\sqrt{\sigma_z(\sigma_x, \sigma_y)}. \qquad (33)$$

The square-root factor comes about from taking the amplitude over the flat instrument pupil to the curved object pupil in a way that conserves energy [11]. The checked factors are additional transfer patterns on the lens or, equivalently, account for a non-plane-wave distribution across the entrance pupil. This notation is simply for convenience and does not limit the following results to aplanatic lenses. Using these forms, Eq. (29) becomes

$$\widetilde{h}_{\alpha\beta}(-\mathbf{Q}_\parallel, -z;k) = -4\pi^2 k\mu_r|P(k)|^2 \int \frac{\check{F}_\alpha\left(\dfrac{\mathbf{q}_\parallel}{k}\right)\check{G}_\beta\left(\dfrac{\mathbf{Q}_\parallel - \mathbf{q}_\parallel}{k}\right)}{\sqrt{k_z(\mathbf{q}_\parallel)}\ \sqrt{k_z(\mathbf{Q}_\parallel - \mathbf{q}_\parallel)}}$$

$$\times e^{i[k_z(\mathbf{q}_\parallel) + k_z(\mathbf{Q}_\parallel - \mathbf{q}_\parallel)]z}\mathrm{d}^2 q_\parallel. \qquad (34)$$

Assume $\check{F}_\alpha(\mathbf{q}_\parallel/k)\check{G}_\beta((\mathbf{Q}_\parallel - \mathbf{q}_\parallel)/k)$ is peaked at about $\mathbf{q}_\parallel^{(p)}$. Then it is sensible that the integrand modulo of this factor be written as a Taylor series about this point:

$$\frac{e^{i[k_z(\mathbf{q}_\parallel) + k_z(\mathbf{Q}_\parallel - \mathbf{q}_\parallel)]z}}{\sqrt{k_z(\mathbf{q}_\parallel)k_z(\mathbf{Q}_\parallel - \mathbf{q}_\parallel)}} = \sum_{l=0}^\infty \sum_{m=0}^\infty \kappa(l, m, \mathbf{q}_\parallel^{(p)};k)(q_x - q_x^{(p)})^l$$

$$\times (q_y - q_y^{(p)})^m, \qquad (35)$$

where

$$\kappa(l, m, \mathbf{q}_\parallel^{(p)};k) = \left. \frac{\partial^{(l+m)}}{\partial q_x^l \partial q_y^m}\frac{e^{i[k_z(\mathbf{q}_\parallel) + k_z(\mathbf{Q}_\parallel - \mathbf{q}_\parallel)]z}}{\sqrt{k_z(\mathbf{q}_\parallel)k_z(\mathbf{Q}_\parallel - \mathbf{q}_\parallel)}}\right|_{\mathbf{q}_\parallel = \mathbf{q}_\parallel^{(p)}}. \qquad (36)$$

This gives an expansion of Eq. (34) in terms of the moments of $\check{F}_\alpha(\mathbf{q}_\parallel/k)\check{G}_\beta((\mathbf{Q}_\parallel - \mathbf{q}_\parallel)/k)$ as

$$\widetilde{h}_{\alpha\beta}(-\mathbf{Q}_\parallel, -z;k) = -4\pi^2 k\mu_r|P(k)|^2 \sum_{l=0}^\infty \sum_{m=0}^\infty \kappa(l, m, \mathbf{q}_\parallel^{(p)};k)$$

$$\times \int \check{F}_\alpha\left(\frac{\mathbf{q}_\parallel}{k}\right)\check{G}_\beta\left(\frac{\mathbf{Q}_\parallel - \mathbf{q}_\parallel}{k}\right)$$

$$\times (q_x - q_x^{(p)})^l(q_y - q_y^{(p)})^m\mathrm{d}^2 q_\parallel. \qquad (37)$$

As seen in Eq. (36), the derivatives of the exponential de-

termine $\kappa(l, m, \mathbf{q}_\parallel^{(p)};k)$, and so this coefficient decreases more rapidly, with l and m, for low $|kz|$. Similarly, the moments of the aperture functions decay more rapidly for more peaked profiles, i.e., for small NA^2. As a result, the series given in Eq. (37) decays more rapidly for small values of $NA^2|kz|$. Assuming sufficiently small $NA^2|kz|$, the first term in the series dominates:

$$\widetilde{h}_{\alpha\beta}(-\mathbf{Q}_\parallel, -z;k) \approx -4\pi^2 k\mu_r|P(k)|^2\frac{e^{i[k_z(\mathbf{q}_\parallel^{(p)}) + k_z(\mathbf{Q}_\parallel - \mathbf{q}_\parallel^{(p)})]z}}{\sqrt{k_z(\mathbf{q}_\parallel^{(p)})k_z(\mathbf{Q}_\parallel - \mathbf{q}_\parallel^{(p)})}}$$

$$\times \int \check{F}_\alpha\left(\frac{\mathbf{q}_\parallel}{k}\right)\check{G}_\beta\left(\frac{\mathbf{Q}_\parallel - \mathbf{q}_\parallel}{k}\right)\mathrm{d}^2 q_\parallel. \qquad (38)$$

The condition of small $NA^2|kz|$ required here, in the near-focus case, is in direct opposition to the far-from-focus case where $NA^2|kz|$ must be large.

In many cases of interest, $\check{F}_\alpha(\mathbf{q}_\parallel/k)$ and $\check{G}_\beta(\mathbf{q}_\parallel/k)$ are circularly symmetric and equal. Then it is most sensible to make the expansion about the point $\mathbf{q}_\parallel^{(p)} = \mathbf{Q}_\parallel/2$ as was done in [6]. This particular point also results in $\kappa(1, 0, \mathbf{Q}_\parallel/2;k) = \kappa(0, 1, \mathbf{Q}_\parallel/2;k) = \kappa(1, 1, \mathbf{Q}_\parallel/2;k) = 0$, so that the approximation is accurate up to second-order terms. This expansion point will be chosen for the remainder of this work, resulting in the near-focus model

$$\widetilde{h}_{\alpha\beta}(-\mathbf{Q}_\parallel, -z;k) \approx -4\pi^2 k\mu_r|P(k)|^2\frac{K_{\alpha\beta}(\mathbf{Q}_\parallel;k)}{k_z(\mathbf{Q}_\parallel/2)}e^{i2k_z(\mathbf{Q}_\parallel/2)z}, \qquad (39)$$

where

$$K_{\alpha\beta}(\mathbf{Q}_\parallel;k) = \int \check{F}_\alpha\left(\frac{\mathbf{q}_\parallel}{k}\right)\check{G}_\beta\left(\frac{\mathbf{Q}_\parallel - \mathbf{q}_\parallel}{k}\right)\mathrm{d}^2 q_\parallel. \qquad (40)$$

An example of the evaluation of $K_{\alpha\beta}(\mathbf{Q}_\parallel;k)$ is given in Subsection 3.E. In contrast to the far-from-focus approximation, the near-focus result cannot be cast in a geometrical optics framework, as the fields in the focal region are dependent upon the entire aperture. The diffraction effects in the focal region cannot be modeled using ray optics.

While the expansion around $\mathbf{q}_\parallel^{(p)} = \mathbf{Q}_\parallel/2$ is applicable in many cases, it is easy to envision a scenario where it is not. Consider an example where $\check{F}_\alpha(\mathbf{q}_\parallel/k)$ is a radially symmetric Gaussian with variance s_1^2 and $\check{G}_\beta(\mathbf{q}_\parallel/k)$ is a radially symmetric Gaussian with variance s_2^2. In this case $\check{F}_\alpha(\mathbf{q}_\parallel/k)\check{G}_\beta((\mathbf{Q}_\parallel - \mathbf{q}_\parallel)/k)$ can be shown to be centered around $\mathbf{q}_\parallel^{(p)} = \mathbf{Q}_\parallel \mathsf{s}_1^2/(\mathsf{s}_1^2 + \mathsf{s}_2^2)$.

D. Unified Approximated Model

The near-focus and far-from-focus approximations of Eqs. (31) and (39) can both be written in the form

$$\widetilde{h}_{\alpha\beta}(-\mathbf{Q}_\parallel, -z;k) \approx H_{\alpha\beta}(\mathbf{Q}_\parallel;k)\rho(z)e^{i2k_z(\mathbf{Q}_\parallel/2)z}, \qquad (41)$$

where

$$H_{\alpha\beta}(\mathbf{Q}_\parallel;k) = \begin{cases} H_{\alpha\beta}^{(N)}(\mathbf{Q}_\parallel;k) = -4\pi^2 k\mu_r|P(k)|^2\dfrac{K_{\alpha\beta}(\mathbf{Q}_\parallel;k)}{k_z(\mathbf{Q}_\parallel/2)} & |z| \ll \dfrac{1}{kNA^2} \\[14pt] H_{\alpha\beta}^{(F)}(\mathbf{Q}_\parallel;k) = i4\pi^3 k_z(\mathbf{Q}_\parallel/2)\mu_r|P(k)|^2\check{F}_\alpha\!\left(\dfrac{\mathbf{Q}_\parallel/2}{k}\right)\check{G}_\beta\!\left(\dfrac{\mathbf{Q}_\parallel/2}{k}\right) & |z| \gg \dfrac{1}{kNA^2} \end{cases}, \tag{42}$$

$$\rho(z) = \begin{cases} \rho^{(N)}(z) = 1 & |z| \ll \dfrac{1}{kNA^2} \\[12pt] \rho^{(F)}(z) = \dfrac{1}{z} & |z| \gg \dfrac{1}{kNA^2} \end{cases}. \tag{43}$$

Note that the far-from-focus approximation in Eq. (42) has been rewritten in terms of the aplanatic-lens profiles given in Eqs. (32) and (33). It can also be seen that as z moves from a large negative value to zero to a large positive value, the phase of $H_{\alpha\beta}(\mathbf{Q}_\parallel;k)$ changes from $3\pi/2$ to π to $\pi/2$—this behavior is analogous to the well-known phase anomaly, or Gouy phase shift, observed in a focused beam (see [25], Chapter 8.8.4).

The conditions on z in Eqs. (42) and (43) make it clear that Eq. (41) is valid only in the near-focus and far-from-focus regions, not necessarily in the intermediate zone. Also note that the intermediate zone's location is a function of k and thus varies within a single data set. However, the image-reconstruction procedure developed in Section 3 will assume a model of the form given in Eq. (41) over all space. Although this approximation is not rigorously justified, numerical simulations will show that it allows excellent image reconstruction using a very simple algorithm.

This form for the model makes evident the effects of coherent imaging as three separate phenomena. The beam profiles, polarization behavior, aberrations, and other such lens-determined or user-defined effects are expressed in $H_{\alpha\beta}(\mathbf{Q}_\parallel;k)$, while the decay in signal away from the focus is expressed by $\rho(z)$. The broadening effect of defocusing is represented in the complex exponential factor, which can be seen by noting that the only other z dependence present is in $\rho(z)$, and this is just a loss in signal strength. So the fact that the shape of the point-spread function varies with z is due solely to the complex exponential. Restated, it is known that $h_{\alpha\beta}(\mathbf{r}_\parallel,z)$ becomes broader, due to defocus, as z moves away from the $z=0$ focal plane. This effect is due solely to the exponential factor in Eq. (41). This exponential factor is identical in both the near-focus and far-from-focus approximations.

This unified form for the approximation shows how defocusing effects can be decoupled from the wide range of other factors that influence the performance of a coherent imaging system. Near-focus and far-from-focus scatterers are both shown to be subject to the same phase-shifting effect. The border between the near-focus and the far-from-focus regions will be explored further in subsequent sections. In the next section the scalar Gaussian case is considered, and it is shown that the exact analytic expression for this case has a clear relation to the two approximations developed in this section.

E. Scalar Gaussian Case

For systems of low NA, the fields $\mathbf{g}(\mathbf{r}-\mathbf{r}^{(o)};k)$ and $\mathbf{f}(\mathbf{r}-\mathbf{r}^{(o)};k)$ will be dominated by one polarization state. For example, if in the incident field $\mathbf{E}^{(i)}$ is x polarized and the lens is of low NA and made of an isotropic material, the field $\mathbf{g}(\mathbf{r}-\mathbf{r}^{(o)};k)$ will be predominantly x polarized. This is because each nonzero component of its plane-wave spectrum is traveling at a small angle to the optic axis. The consequence of this uniform polarization is that only one (α,β) pair in Eq. (14) will produce a significant point-spread function. Thus the sum of Eq. (13) reduces to a single term, and scalar optics can be applied. This low-NA/scalar treatment of the focused field is consistent with the paraxial treatment of the Helmholtz equation. Gaussian beams are a solution to this equation and are widely used to model focused light. In the remainder of this section, the techniques developed here are compared with standard scalar, Gaussian analysis.

Consider the scalar case where the field incident on the lens is

$$e^{-\gamma^2(x^2+y^2)/(2\zeta^2)}, \tag{44}$$

where the width of this function is determined by γ and ζ is the lens focal length. The distribution on the object-side pupil can then be given by the expression

$$\check{G}(\sigma_x,\sigma_y) = e^{-\gamma^2(\sigma_x^2+\sigma_y^2)/2}. \tag{45}$$

This form assumes an aplanatic lens as each ray emerges from its input height. The factor $\sqrt{\sigma_z(\sigma_x,\sigma_y)}$ is required to conserve energy and is implied in Eq. (33). The NA of the lens can then be defined in terms of γ as

$$\gamma = \sqrt{2}/NA. \tag{46}$$

The NA for the Gaussian beam is the sine of the angle at which the distribution at the object-side pupil drops to $1/e$ of its maximum.

Since a single objective lens is being used, Eq. (15) is satisfied, and since a scalar case is being considered, matching the polarizations, as in Eq. (16), is not an issue. This gives

$$\check{F}(\sigma_x,\sigma_y) = e^{-\gamma^2(\sigma_x^2+\sigma_y^2)/2}. \tag{47}$$

The far-from-focus approximation of Eq. (31) can now be evaluated. The near-focus approximation can also be found by first calculating $K(\mathbf{Q}_\parallel;k)$ using Eq. (40):

$$K(\mathbf{Q}_{\parallel};k) = \int e^{-\gamma^2(q_x^2+q_y^2)/(2k^2)}e^{-\gamma^2((Q_x-q_x)^2+(Q_y-q_y)^2)/(2k^2)}\mathrm{d}\mathbf{q}_{\parallel}$$

$$= \int e^{-\gamma^2(Q_x^2+Q_y^2)/(4k^2)}e^{-\gamma^2((q_x-Q_x/2)^2+(q_y-Q_y/2)^2)/k^2}\mathrm{d}\mathbf{q}_{\parallel}$$

$$= (e^{-\gamma^2\{[Q_x/(2k)]^2+[Q_y/(2k)]^2\}/2})2\frac{\pi k^2}{\gamma^2}$$

$$= \frac{\pi k^2}{\gamma^2}\check{F}\left(\frac{\mathbf{Q}_{\parallel}/2}{k}\right)\check{G}\left(\frac{\mathbf{Q}_{\parallel}/2}{k}\right). \tag{48}$$

The model is now defined by Eqs. (41)–(43) with the following definitions:

$$H^{(N)}(\mathbf{Q}_{\parallel};k) = -4\pi^3k^3\mu_r|P(k)|^2\frac{1}{\gamma^2k_z(\mathbf{Q}_{\parallel}/2)}\check{F}\left(\frac{\mathbf{Q}_{\parallel}/2}{k}\right)\check{G}\left(\frac{\mathbf{Q}_{\parallel}/2}{k}\right), \tag{49}$$

$$H^{(F)}(\mathbf{Q}_{\parallel};k) = i4\pi^3k_z(\mathbf{Q}_{\parallel}/2)\mu_r|P(k)|^2\check{F}\left(\frac{\mathbf{Q}_{\parallel}/2}{k}\right)\check{G}\left(\frac{\mathbf{Q}_{\parallel}/2}{k}\right). \tag{50}$$

This scalar Gaussian case has been examined in the literature. The unapproximated outcome shown in [5] in Eq. (3.23) can be restated in a form relevant to the results derived here:

$$\tilde{h}(-\mathbf{Q}_{\parallel},-z;k) = \left[\frac{1}{H^{(N)}(\mathbf{Q}_{\parallel};k)\rho^{(N)}(z)}\right.$$
$$\left. + \frac{1}{H^{(F)}(\mathbf{Q}_{\parallel};k)\rho^{(F)}(z)}\right]^{-1}e^{i2k_z(\mathbf{Q}_{\parallel}/2)z}. \tag{51}$$

The equation above comes from [5] after accounting for paraxial approximations, differing representations of the angular spectra, and correcting a factor of k that is incorrectly dropped between Eqs. (3.18) and (3.23).

A method of transitioning between the near-focus and the far-from-focus approximations is given in Eq. (51). It can be seen that at large z the far-from-focus result dominates and that at low z the near-focus result dominates due to the form of $\rho(z)$ [Eq. (43)]. From Eq. (51) it can be seen that the approximation to the exact model derived in this work is clearly related to an exact result for one particular approximated (i.e., scalar and Gaussian) system.

The transition point between the near-focus and the far-from-focus regimes can also be evaluated in Eq. (51). The point at which both the terms contribute equally is

$$|z| = \frac{\gamma^2k_z^2(\mathbf{Q}_{\parallel}/2)}{k^3} \approx \frac{\gamma^2}{k} = \frac{2}{kNA^2} = \frac{\lambda}{\pi NA^2}. \tag{52}$$

This transition point is where $|z|$ is one Rayleigh range ($NA^2|kz|=2$). Physically, this indicates that the near-focus approximation is valid when the field is well collimated, while the far-from-focus approximation is valid when the field is behaving as a spherical wave.

4. IMAGE RECONSTRUCTION
In this section, the problem of constructing an image of the susceptibility from the data is addressed. It will be

shown that the defocusing portion of the model can be cast as Fourier-domain resampling. This suggests a simple reconstruction method.

The approximate kernel of Eq. (41) is substituted into the observation model of Eq. (21). It is assumed, without loss of generality, that the origin of the coordinate system lies in the focal plane so that $z^{(o)}=0$, then

$$\tilde{S}(\mathbf{Q}_{\parallel},k) = H_{\alpha\beta}(-\mathbf{Q}_{\parallel};k)\int\rho(z)\tilde{\eta}_{\alpha\beta}(\mathbf{Q}_{\parallel},z)e^{i2k_z(-\mathbf{Q}_{\parallel}/2)z}\mathrm{d}z. \tag{53}$$

It is useful to define a modified susceptibility as

$$\overline{\boldsymbol{\eta}}'(\mathbf{r}) = \rho(z)\overline{\boldsymbol{\eta}}(\mathbf{r}). \tag{54}$$

Using this susceptibility and the fact that $k_z(-\mathbf{Q}_{\parallel}/2) = k_z(\mathbf{Q}_{\parallel}/2)$ yields

$$\tilde{S}(\mathbf{Q}_{\parallel},k) = H_{\alpha\beta}(-\mathbf{Q}_{\parallel};k)\int\tilde{\eta}'_{\alpha\beta}(\mathbf{Q}_{\parallel},z)e^{i2k_z(\mathbf{Q}_{\parallel}/2)z}\mathrm{d}z. \tag{55}$$

The integral above can be recognized as a Fourier transform in the z dimension. Let $\approx$ denote a three-dimensional Fourier transform, so that

$$\tilde{S}(\mathbf{Q}_{\parallel},k) = H_{\alpha\beta}(-\mathbf{Q}_{\parallel};k)\tilde{\tilde{\eta}}'_{\alpha\beta}(\mathbf{Q}_{\parallel},-2k_z(\mathbf{Q}_{\parallel}/2)). \tag{56}$$

This equation relates the data at lateral spatial frequency $\mathbf{Q}_{\parallel}$ and wavenumber k to the three-dimensional Fourier transform of the susceptibility. This relationship, between the data collected at $(\mathbf{Q}_{\parallel},k)$ and the object's Fourier representation at $\mathbf{Q}=(\mathbf{Q}_{\parallel},Q_z)$, is illustrated graphically in Fig. 3. The Fourier relation in Eq. (56) is a generalization of the scalar Gaussian result presented in an earlier paper on high-NA ISAM [6]; however, that result was de-
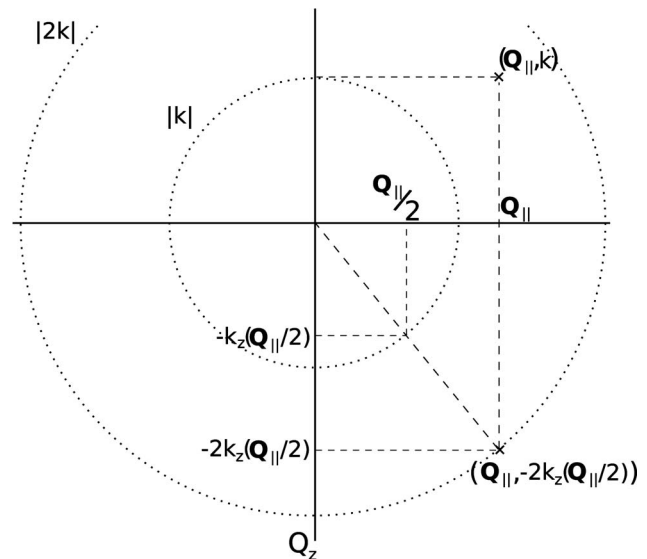

Fig. 3. Illustration of the Fourier-domain relation between the collected data and the object. A point $(\mathbf{Q}_{\parallel},k)$ in the data corresponds to the point $\mathbf{Q}=(\mathbf{Q}_{\parallel},-2k_z(\mathbf{Q}_{\parallel}/2))$ in the Fourier-domain representation of the object. Thus the two-dimensional Fourier transform of the data at wavenumber k gives the object's three-dimensional Fourier components at the same lateral frequencies and at a distance of $2k$ from the origin.

rived based solely on approximations valid in the near-focus region. It is a fortunate happenstance that the near-focus and far-from-focus cases produce the same Fourier resampling when equal circularly symmetric lens-aperture functions are used. The Fourier mapping seen in Fig. 3 also arises in SAR, where it is often known as the Stolt mapping [27].

In traditional Fourier-domain OCT, the object is estimated by simply taking the Fourier transform of the data along the k dimension. This takes the spectral-OCT data into the spatial domain. The resulting image is known to be stretched by a factor of -2 in the axial direction. This image-reconstruction technique is equivalent to assuming the point $(\mathbf{Q}_\parallel, k)$ in the data corresponds to the point $\mathbf{Q} = (\mathbf{Q}_\parallel, -2k)$ in the three-dimensional Fourier representation of the object. It will be seen that correcting $(\mathbf{Q}_\parallel, -2k)$ to $(\mathbf{Q}_\parallel, -2k_z(\mathbf{Q}_\parallel/2))$ will provide significant advantages.

The effects of $H_{\alpha\beta}(\mathbf{Q}_\parallel; k)$ could be mitigated by applying a regularized inverse filter, e.g., a Wiener filter [28]. However, this portion of the forward model depends on system parameters such as the beam profile used, the polarization states chosen, etc. It is also dependent on whether a scatterer is in the near-focus or out-of-focus regime. For these reasons, its effects will not be inverted at this point. As mentioned earlier, the defocusing effect is contained in the complex exponential factor in Eq. (41) and that is what will be inverted here. Since $H_{\alpha\beta}(\mathbf{Q}_\parallel; k)$ is a smooth (within the passband), real (in the aberration-free case) Fourier-domain weighting, it represents simple linear shift-invariant filtering that will not introduce major distortions to the image. However, it should be noted that in polarization-sensitive imaging techniques, the $H_{\alpha\beta}(\mathbf{Q}_\parallel; k)$ factor will be important, since how it changes with α and β determines the polarization response of the system.

In Subsection 2.C it was assumed that the susceptibility of a scatterer was constant over the wavenumbers observed. If it is not, the variation with k will have an effect similar to that of the factor $H_{\alpha\beta}(\mathbf{Q}_\parallel; k)$. In fact, if the k dependence is known and spatially uniform across the object, as would occur when only one well-characterized scattering material is present, it can be incorporated into $H_{\alpha\beta}(\mathbf{Q}_\parallel; k)$ and compensated. In cases where the susceptibility varies as a nonseparable function of space and observed wavenumber and/or is not known *a priori*, distortions may occur in the image. The wavenumber variation results in a Fourier-domain modulation of the data from each scatterer. In cases where the wavenumber variation is slow, the resulting image distortion can be expected to be minor. However, if a rapid spectral change in susceptibility amplitude and/or phase is present, the reconstruction quality may be significantly compromised. Such distortions would also occur in OCT imaging but can be expected to be more detrimental in the phase-sensitive out-of-focus reconstructions performed as part of the ISAM method. This issue will be more pressing for large-bandwidth imaging systems.

The factor $\rho(z)$ in Eq. (41) is a z-dependent scaling, but for three-dimensional image display, it is useful to have some means of inverting its effects. Consistent with Eq. (43), an approximated form will be used to model the axial decay of the signal:

$$\varrho(z) = \begin{cases} 1 & |z| < z^{(c)} \\ z^{(c)}/z & |z| \geq z^{(c)} \end{cases} . \tag{57}$$

In this approximation $z^{(c)}$ represents the axial plane at which the model moves from the near-focus to the out-of-focus regimes. The factor of $z^{(c)}$ in the second term is included to ensure continuity. The image recovered after Fourier resampling will be divided by this function in order to retrieve an estimate of $\overline{\eta}(\mathbf{r})$ from the estimate of $\overline{\eta}'(\mathbf{r})$ given [Eq. (54)]. As mentioned in Subsection 3.D this procedure is not rigorously justified for the intermediate area between near-focus and far-from-focus scatterers; however, in each limit the same resampling procedure is suggested. The numerical simulations in the next section also show good performance at all axial positions when this inversion method is applied. Additionally, the form given in Eq. (57) will be further justified in Subsection 5.C.

The ISAM image-reconstruction algorithm presented here is noniterative and nonadaptive and can be implemented computationally using only the Fourier transform, interpolation, and multiplication. Fast and efficient algorithms exist for all of these operations, resulting in a reconstruction procedure that can be readily implemented on a modern personal computer.

5. NUMERICAL SIMULATIONS

The numerical simulations in this section apply the reconstruction approach of Section 4 to data simulated using the unapproximated forward model of Section 2. The results demonstrate the validity of the approximations derived in Section 3 and the advantages that can be expected by using ISAM processing.

A. Simulation Parameters

This section will present numerical simulations where the data are generated using the exact model in the form of Eq. (17) and the reconstructions are calculated using the algorithm proposed in Section 4. Various NAs are considered, and the lens is assumed to be illuminated by an x-polarized plane wave. The detection polarization $\mathbf{E}^{(d)}$ is also assumed to be linearly polarized in the x direction. The illumination amplitude $P(k)$ will be set to $1/(kNA)$ to compensate for the wavenumber-dependent scattering strength described in Subsection 2.C and so that the integrated intensity of the sample-arm light over the lens is preserved with NA. The reference amplitude will be kept constant with NA by setting $\mu_r = NA$. Isotropic scattering is assumed so that the susceptibility is scalar:

$$\overline{\boldsymbol{\eta}}(\mathbf{r}) = \eta(\mathbf{r}) \begin{bmatrix} 1 & 0 & 0 \\ 0 & 1 & 0 \\ 0 & 0 & 1 \end{bmatrix}. \tag{58}$$

Substituting this expression for $\overline{\boldsymbol{\eta}}(\mathbf{r})$ into Eq. (56), it is found that

$$\widetilde{S}(\mathbf{Q}_\parallel; k) = \left(\sum_\alpha H_{\alpha\alpha}(-\mathbf{Q}_\parallel; k) \right) \tilde{\eta}'(\mathbf{Q}_\parallel, -2k_z(\mathbf{Q}_\parallel/2)), \tag{59}$$

where

$$\eta'(\mathbf{r}) = \rho(z)\,\eta(\mathbf{r}). \tag{60}$$

Two image-reconstruction techniques will be considered. The first is the traditional approach of taking the fast Fourier transform (FFT) of spectral-domain data over the k dimension and correcting for the axial scaling of -2 in the reconstructed image (as mentioned in Section 4). The second approach will be to use the resampling method described in Section 4 and illustrated in Fig. 3. A two-dimensional Fourier transform over $\mathbf{r}_\parallel$ will be applied to the data $S(\mathbf{r}_\parallel, k)$ and the resulting $(\mathbf{Q}_\parallel, k)$ data points shifted to $(\mathbf{Q}_\parallel, -2k_z(\mathbf{Q}_\parallel/2))$. A three-dimensional inverse FFT is then applied to get an estimate of $\eta'(\mathbf{r})$. For both methods the approximated axial response $\varrho(z)$ [Eq. (57)] is divided out and the magnitude of the result is plotted as the reconstructed image.

B. One-Scatterer Simulations

Consider a unit-amplitude point scatterer located on the z axis. In Fig. 4, the results of the simulated imaging of three such objects are shown. Axial offsets of 1 μm, 2 μm, and 5 μm are considered for a system using a lens with a NA of 0.75. This high NA serves to effectively demonstrate the results of the resampling scheme and also to illustrate that image reconstruction with such high NAs is
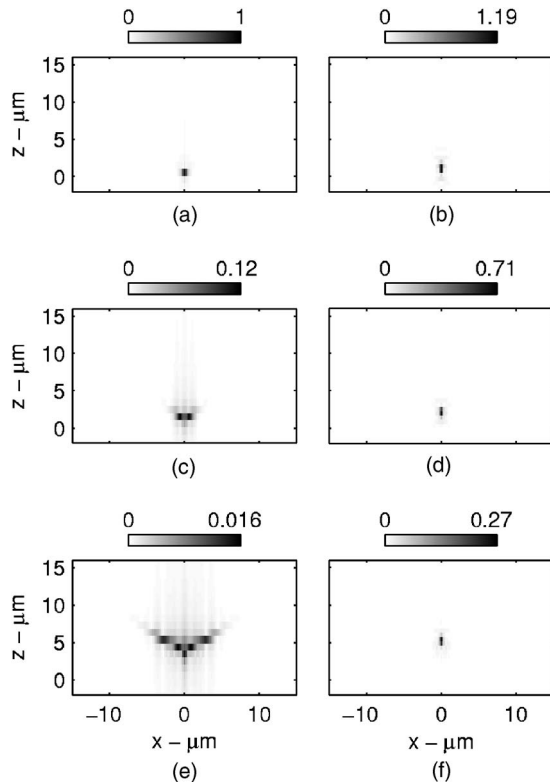

Fig. 4. Reconstructed images for point scatterers lying on the z axis. Images (a), (c), and (e) show standard reconstructions, while (b), (d), and (f) show ISAM resampling-based reconstructions. Images (a) and (b) correspond to a scatterer at $(0,0,1)$ μm, (c) and (d) are for a scatterer at $(0,0,2)$ μm, and (e) and (f) are for a scatterer at position $(0,0,5)$ μm. The two-dimensional plots shown are a lateral-axial slice of the respective three-dimensional reconstructions. The images are plotted in normalized units, where the peak value of (a) is 1. Note the drop in signal as the z position of the scatterer increases.
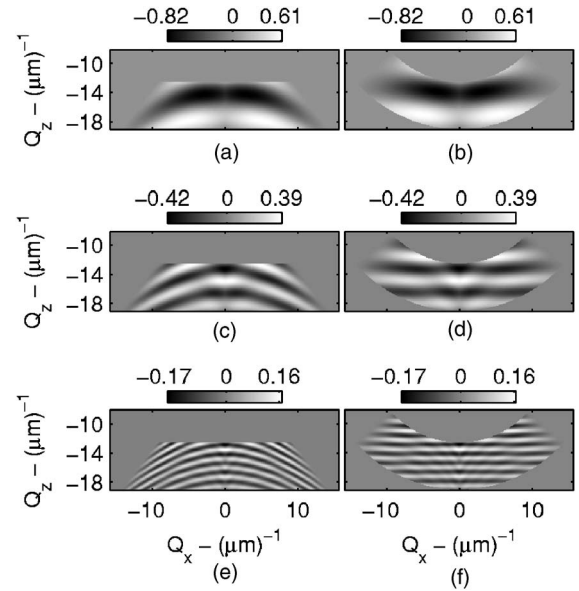

Fig. 5. Real part of the Fourier-domain representations of the reconstructions from Fig. 4. The standard OCT reconstructions, shown on the left, stretch the Fourier representation of the data by a factor of 2 axially and flip the axial Fourier axis. The ISAM resampling approach (results shown on the right) can be seen to correct the data so as to better match the expected Fourier spectra of the object. In this case the Fourier-domain objects are complex exponentials oscillating in the axial direction—i.e., the oscillation crests should be straight.

possible. Three-dimensional data are collected for 64 evenly spaced wavenumbers between 6.28 μm^{-1} (1000 nm wavelength in free space) and 9.52 μm^{-1} (660 nm). At each wavelength a 256×256 image is collected, where each pixel corresponds to a 200 nm $\times$ 200 nm area in the object. A traditional reconstruction is shown for each object along with a reconstruction based on Fourier resampling (as described above). The axial signal decay is not compensated in these reconstructions.

It can be seen from Fig. 4 that the resampling-based approach does an excellent job of restoring the out-of-focus scatterers. The reason for this is clear when the reconstructions are examined in the Fourier domain. The Fourier transforms of these axially offset scatterers are complex exponentials oscillating in the Q_z direction. The frequency of oscillation corresponds to the axial offset. As can be seen from Fig. 5, the observation distorts these straight oscillations to a curved path. Spatially, the bending of the phase fronts corresponds to an out-of-focus blurring. When the proposed image-reconstruction algorithm is applied, the previously curved paths are straightened within what is now a curved passband. The spatial effect is to bring the previously out-of-focus points into sharp contrast. The reconstructions can still be seen to drop in intensity with $|z|$. This is due to the fact that $\eta'(\mathbf{r})$ [Eq. (60)] is being estimated and that its strength is predicted to drop with $|z|$ as dictated by $\rho(z)$.

As can be seen in Fig. 5, the curves are not corrected to exactly straight lines. This is due to the approximations used in Section 3. Additionally, the amplitude of the complex oscillations is not entirely uniform throughout the passband. This can be attributed to the $H_{\alpha\alpha}(\mathbf{Q}_\parallel; k)$ factor of Eq. (59). The phase fronts appear straighter for the

5 μm scatterer as the stationary-phase approximation becomes more accurate as $|z|$ increases. For this system the Rayleigh range [as defined in Eq. (52)] is approximately 0.5 μm, so the scatterers of Figs. 4 and 5 are either in the transition or out-of-focus regime. The spectral oscillations of something closer to the focal point would be hard to see across the passband and so are not included in these simple simulations. Later results illustrate the transition between near-focus and far-from-focus and also include reconstructions of near-focus points.

C. Determining the Near-Focus-to-Out-of-Focus Transition

From Eq. (42) it can be seen that the signal level is z dependent for out-of-focus scatterers but not for near-focus scatterers. This fact can be used to numerically determine the boundary between these two regions. The forward model can be used to calculate the total intensity incident on the detector plane for any given scatterer. A number of scatterers at various positions along the optic axis were considered, and the resulting intensities are plotted in Fig. 6.

Using Parseval's theorem and the expressions in Eq. (42), the expected intensity can be calculated. From such a calculation it can be seen that the intensity should decay as z^{-2} far from focus. This can be seen in Fig. 6 as a slope of -2 is observed on the log–log plot. Additionally, since $P(k)$ was chosen to be inversely proportional to the NA (giving a sample exposure that is constant with NA) and μ_r is proportional to the NA (to give a NA-constant reference), the out-of-focus intensity is independent of the NA. This is also observed in Fig. 6. This result has significant consequences for imaging, as it means that choosing a higher NA does not compromise the signal strength away from focus even though the defocus effects are expected to be severe. That is, not only does ISAM provide a means to recover out-of-focus planes in coherent imaging,

Fig. 7. Noise-free reconstructions of an object consisting of ten point scatterers positioned in the x–z plane at [(5.5,0,0), (0,0,1), (4.5,0,−4.5), (0,0,5), (−2,0,7), (2,0,−15), (−1,0,−15), (2,0,−16), (12,0,17), and (−20,0,25)] μm. The x–z plane of the three-dimensional reconstructions are shown. Reconstructions for the standard OCT method are shown in (a), (c), and (e), while ISAM Fourier-resampling reconstructions are shown in (b), (d), and (f). Both methods include the axial gain function to boost out-of-focus planes. The NA used is 0.2 in (a) and (b), 0.4 in (c) and (d), and 0.75 in (e) and (f). The image scale is normalized to the maximum reconstruction value for the 0.2 NA data.

it also removes a constraint on the system design and suggests that there is no reason not to use the highest-NA lenses available.

The plots of Fig. 6 can also be used to determine the axial signal model $\varrho(z)$. Fitting each log–log plot with a piecewise constant curve constructed from two straight lines is equivalent to finding a scaled version of $\varrho(z)$. This analysis shows that for these curves the transition point $z^{(c)}$ is approximately 1.5 Rayleigh ranges. This is similar to the value of 1 Rayleigh range derived for the scalar Gaussian case. The transition between these two regimes is also fairly sharp in Fig. 6. Another way of modeling the axial decay would be to take the square root of the decay curves of Fig. 6.

D. Multiple-Scatterer and Noisy Simulations

An object consisting of ten point scatterers is considered. The imaging system uses the same specifications given in Subsection 5.B. The resulting noise-free reconstructions are shown in Fig. 7. For the standard OCT reconstructions it can be seen that an increase in NA provides an increase in lateral resolution but lowers the range of z
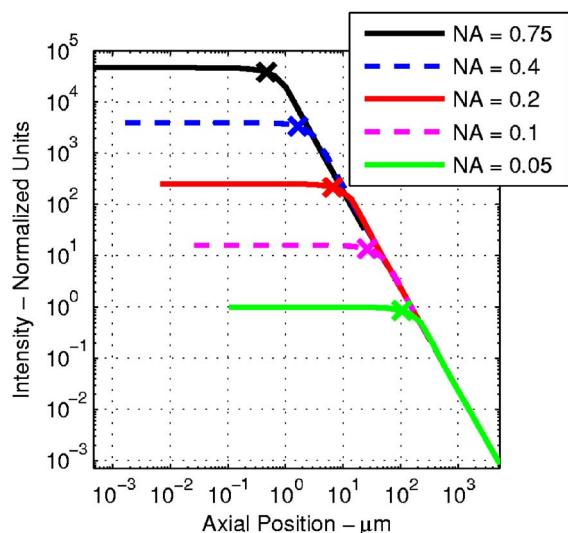

Fig. 6. (Color online) Integral of the intensity falling on the detector plotted for a single scatterer as a function of its axial position. Several NAs are considered, and the intensity is calculated for Rayleigh ranges of 0.001 to 50 with 25 logarithmically spaced points. An ×marks the 1 Rayleigh range point for each plot.

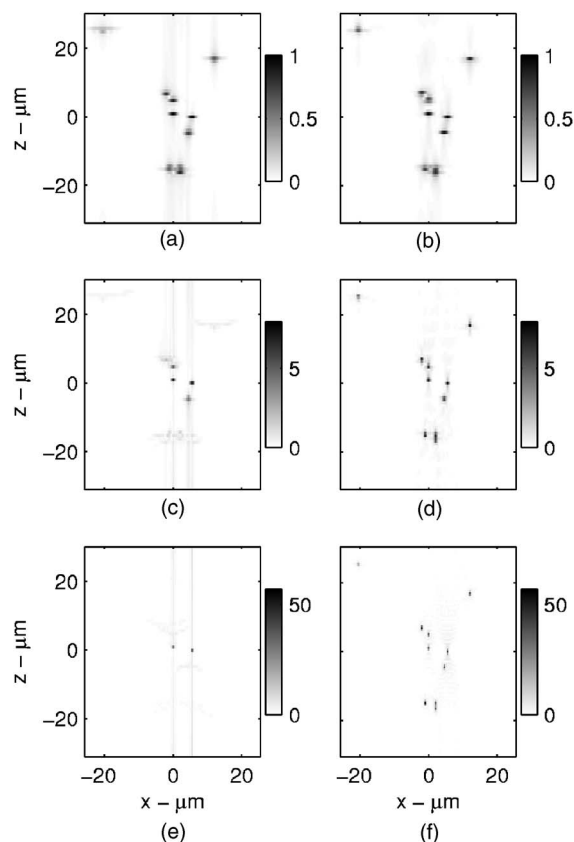that can be imaged without defocusing. By contrast, the ISAM technique both maintains the lateral resolution and compensates for defocusing effects. This is a result similar to that shown in [5] except that a more comprehensive forward model has been used. Vector-field effects, high apertures, and spreading losses are all included in the new model, but the ISAM procedure still produces excellent results.

The 0.2-NA data are largely in focus, so the improvement with ISAM is visible only for the scatterers at the edge of the plot. As the NA is increased, the focal region becomes narrower and the scatterers outside the focal region become invisible in the standard case. ISAM recovers these scatterers well, although the scatterer at $(-20, 0, 25)$ μm does become weaker. This is due to the fact that out-of-focus scatterers will produce a broad spot on the detector in high-NA systems. For scatterers near the border of the imaged region, this means that more of the scattered light will fall outside the detector and that the reconstruction intensity will drop accordingly. Notice that the reconstruction intensity increases with NA. The reconstructions include a gain specified by the reciprocal of $\varrho(z)$. This gain maintains the signal in the focus and amplifies the out-of-focus planes up to a level to match the in-focus signal.

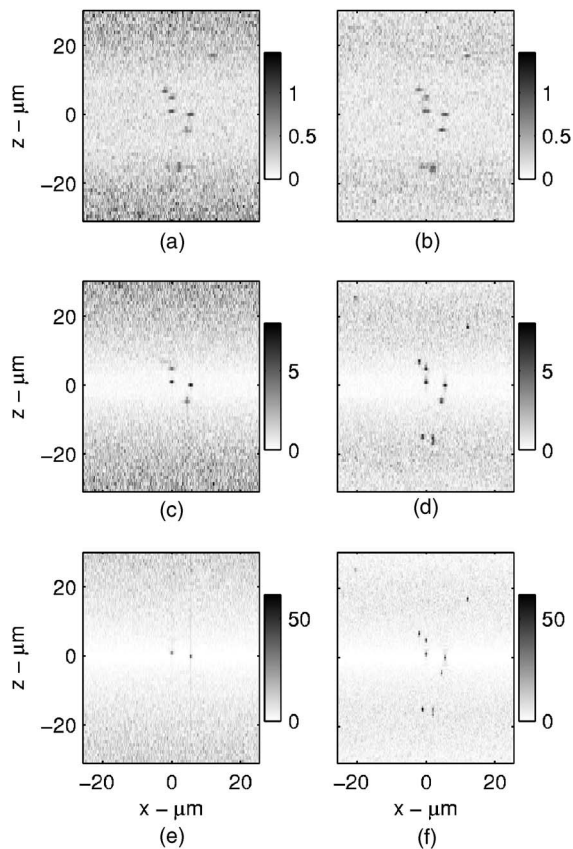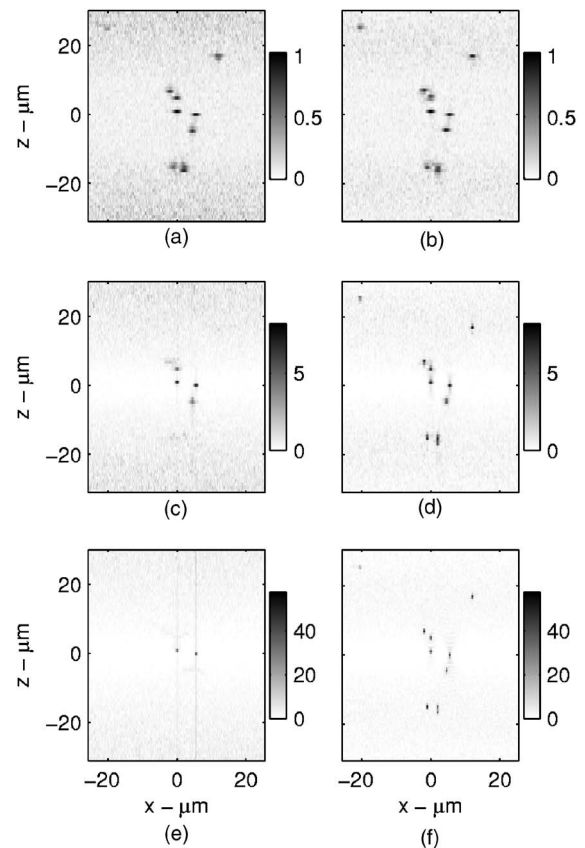Noise was included in the simulated measurements. Complex white Gaussian noise was assumed with vari-

Fig. 9. Noisy reconstructions of the same object considered in Fig. 7, using the same instrument parameters. The noise level considered results in a SNR of 10 dB in the 0.2-NA data. OCT reconstructions are shown on the left and ISAM reconstructions on the right.

Fig. 8. Noisy reconstructions of the same object considered in Fig. 7 using the same instrument parameters. The noise level considered results in a SNR of 0 dB in the 0.2-NA data. OCT reconstructions are shown on the left and ISAM reconstructions on the right.

ance independent of the signal level. This assumption is consistent with an OCT system with noise dominated by shot noise from the reference beam and/or thermal noise from the detector [13]. Reconstructions of the ten-scatterer object for two different noise levels are shown in Figs. 8 and 9.

In both Figs. 8 and 9 the data are preprocessed using a noise-reducing filter. This entails zeroing spatial frequencies outside the system's passband. This filter ensures a fair comparison of noise levels across NA, i.e., meaningless high-frequency noise is removed from low-NA reconstructions. The signal-to-noise-ratio (SNR) measure used is defined by considering the total intensity expected from an in-focus, unit-amplitude scatterer and the variance of the noise at a single pixel before the noise-reduction filter is applied.

The out-of-focus spatial amplification used, i.e., dividing by $\varrho(z)$, also has the effect of amplifying the noise away from the focus, as seen in Figs. 8 and 9. This shows that the ISAM depth of focus will be limited by the noise level rather than the NA. For a very noisy system, the signal level in focus and the noise may be comparable. In this case OCT and ISAM would have a similar achievable depth of focus—in ISAM the computationally focused scatterers away from the focal plane would be overwhelmed by noise. However in less-noisy systems the advantage of ISAM would become clear. The OCT recon-
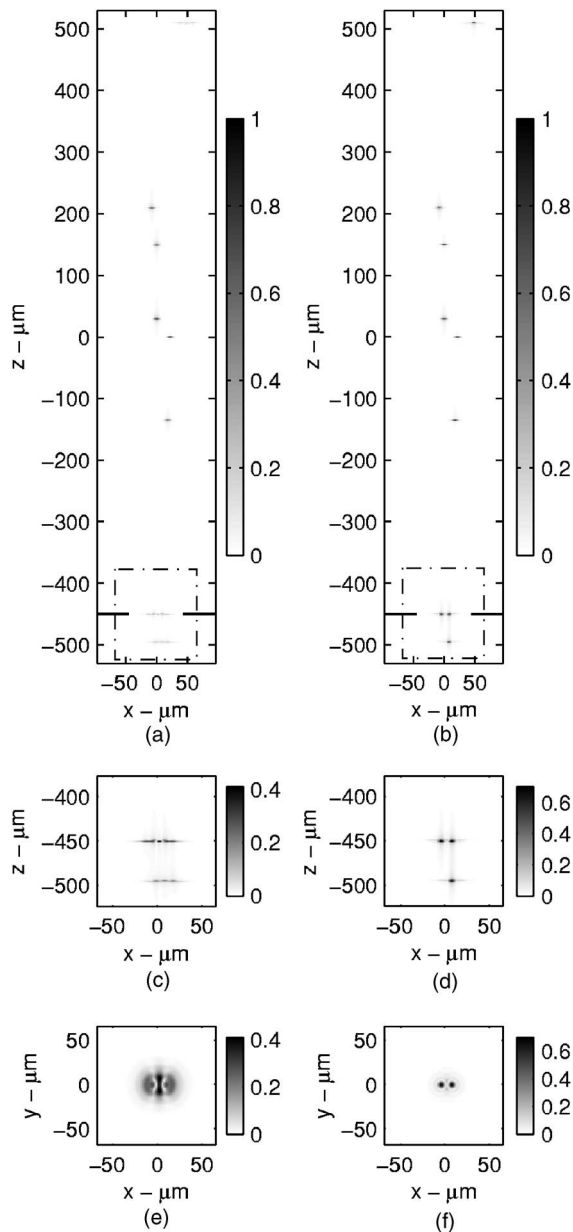
Fig. 10.   Noise-free reconstructions from a 0.05-NA system imaging an object with point scatterers in the $x-z$ plane at positions of [(22,0,0), (0,0,30), (18,0,−135), (0,0,150), (−8,0,210), (8,0,−450), (−4,0,−450), (8,0,−495), and (48,0,510)] μm. The $x-z$ plane of the reconstructions is shown in (a) and (b), along with the $x-z$ detail in (c) and (d) corresponding to the dashed square, and the $x-y$ detail in (e) and (f) from the plane marked with a broken line. Images for the standard OCT method are shown on the left and for the ISAM Fourier-resampling algorithm on the right. Both reconstructions include the axial gain function to boost out-of-focus planes. The image scale is normalized to the maximum reconstruction value.

depth of focus (an exception to this may be for very-low-noise systems, where the signal difference between in-focus and out-of-focus regions may give a dynamic-range-limited depth of focus). For a well-designed OCT/ISAM system and an appropriate sample, it is reasonable to expect a relatively high SNR, as spectral-domain OCT systems have reported sensitivities of greater than 80 dB [13]. Demonstrations of ISAM in tissue have also shown that the SNR is high enough to achieve a significant extension of the useable depth of field [9].

It is interesting to note that in ISAM a high-NA lens does not reduce the depth of focus: A result with important implications for OCM. It can be seen in Fig. 6 that given a constant total intensity incident on the object,
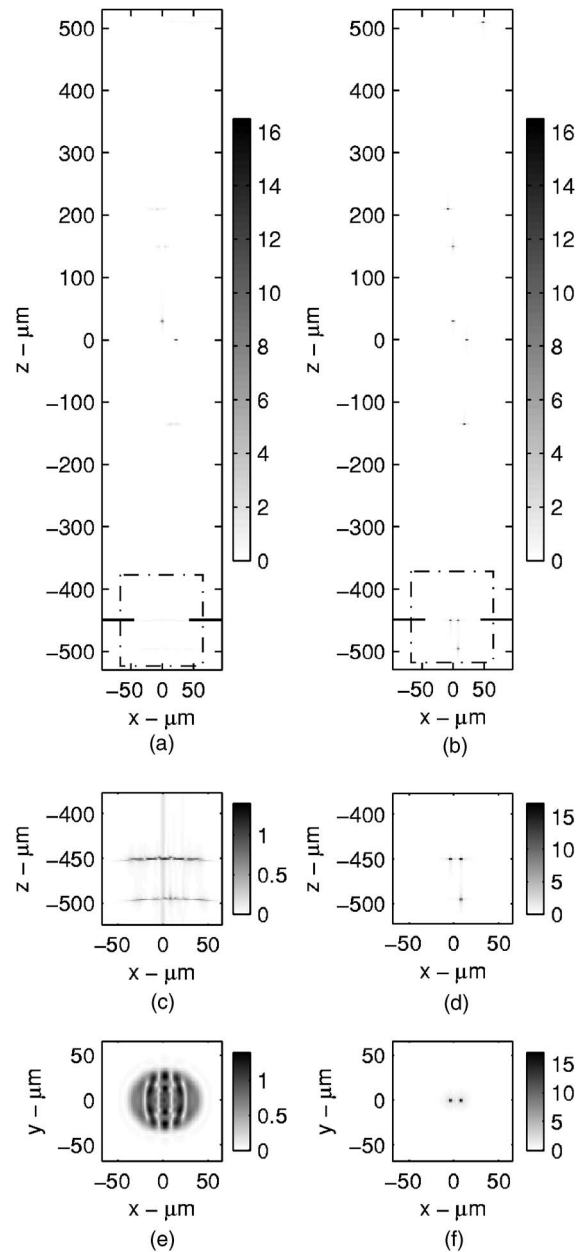

Fig. 11.   Noise-free reconstructions from a 0.1-NA system imaging the object described in Fig. 10. The image scale is normalized to the maximum reconstruction value for the 0.05-NA data. The OCT reconstruction is shown on the left and the ISAM reconstruction on the right.

struction has the traditionally limited depth of field, while the ISAM reconstruction has a uniform resolution. All scatterers in the object would be visible until the axial position at which the $1/|z|$ decay in signal strength results in the scatterer images disappearing under the noise floor. The point at which this occurs can be found by examining Fig. 6. The axial position at which a given noise power exceeds the signal power will give the achievable

varying the NA does not affect the far-from-focus signal strength. This property can also be seen in the reconstructions of Figs. 8 and 9, where the high-NA cases do not suffer from a poorer SNR outside the focal region. Using a high-NA lens also gives an improved lateral resolution. Consequently, OCM need not be limited to *en face* or axially scanned focus methodologies.

ISAM can also be applied to systems of low NA with significant advantage. The ISAM correction of defocus for low-NA data has been demonstrated experimentally [9] and will be examined in simulation here. Consider a system using NAs of 0.05 or 0.1, collecting 1024 wavenumbers evenly spaced between 6.28 μm^{-1} (1000 nm wavelength) and 8.98 μm^{-1} (660 nm wavelength) and with a 128×128 lateral image collected at each wavelength ($1.5~\mu m \times 1.5~\mu m$ pixels). Noise-free reconstructions of a nine-point-scatterer object are shown in Figs. 10 and 11.

The correction of defocus can also be seen in the low-NA images of Figs. 10 and 11. The details for the OCT plots clearly show the blurring associated with defocus and interference effects between two scatterers. The interference effects between scatterers, which are exemplified most clearly in Figs. 10(e) and 11(e), are generally regarded as "speckle" in conventional OCT imaging. ISAM quantitatively infers information about the object structure from the interference effects—this so-called speckle is a useable signal with ISAM processing. It should be noted that speckle may also refer to granular structure in the data resulting from interference effects in multiply scattered light. Since ISAM is based on the first Born (single-scattering) approximation, multiple-scatter speckle remains a nuisance term in ISAM. The Fourier-domain warping used in ISAM does not significantly alter the effective energy content of the signal, so the multiple-scatter speckle and other nuisance terms will not be unduly amplified in the ISAM reconstruction.

6. CONCLUSIONS

A rigorous vectorial model for coherent microscopy was derived without the use of low-angle assumptions such as the paraxial approximation. This model is directly applicable to OCT and OCM. Motivated by these applications, a broadband instrument with a planar scanning geometry was considered, and it was shown that two separate approximations to the model both result in the ISAM image-reconstruction procedure. The two model approximations span the near-focus and far-from-focus regions, but numerical simulations show that ISAM processing produces excellent results at all positions within the imaged object.

ISAM processes the raw data using Fourier-domain resampling. This warping in Fourier space produces a quantitative agreement between the reconstruction and the object imaged. Traditional OCT imaging neglects to correct for Fourier-space distortions introduced by the imaging system, and as a result, defocusing effects distort the image. It was shown that the depth of focusing in planar scanning broadband coherent microscopes is not limited by defocus but rather by noise only. Additionally, increasing the NA of the objective lens does not reduce the depth of focus, it increases only resolution and signal level in the in-focus region.

The model presented here and the resulting inversion techniques provide the tools for quantitative analysis of several other techniques. Any lens aberrations or chromatic behavior can easily be included in the model. The inversion process can then be modified to take these effects into account and compensate for them. The vector analysis presented encompasses polarization-sensitive coherent instruments such as interferometric imaging polarimetry [29], polarized optical coherence imaging [30], and polarization-sensitive OCT [31], so these can also be analyzed using this quantitative model. For example, this work provides a framework for reconstructing the tensor susceptibility for anisotropic scatterers. It is also possible to perform approximation-free image reconstruction using a more computationally expensive approach, as discussed in Subsection 2.F.

REFERENCES

1. T. Wilson and C. J. R. Sheppard, *Theory and Practice of Scanning Optical Microscopy* (Academic, 1984).
2. J. A. Izatt, M. R. Hee, G. M. Owen, E. A. Swanson, and J. G. Fujimoto, "Optical coherence microscopy in scattering media," Opt. Lett. **19**, 590–592 (1994).
3. W. Denk, J. H. Strickler, and W. W. Webb, "Two-photon laser scanning fluorescence microscopy," Science **248**, 73–76 (1990).
4. D. Huang, E. A. Swanson, C. P. Lin, J. S. Schuman, W. G. Stinson, W. Chang, M. R. Hee, T. Flotte, K. Gregory, C. A. Puliafito, and J. G. Fujimoto, "Optical coherence tomography," Science **254**, 1178–1181 (1991).
5. T. S. Ralston, D. L. Marks, P. S. Carney, and S. A. Boppart, "Inverse scattering for optical coherence tomography," J. Opt. Soc. Am. A **23**, 1027–1037 (2006).
6. T. S. Ralston, D. L. Marks, S. A. Boppart, and P. S. Carney, "Inverse scattering for high-resolution interferometric microscopy," Opt. Lett. **24**, 3585–3587 (2006).
7. D. L. Marks, T. S. Ralston, P. S. Carney, and S. A. Boppart, "Inverse scattering for rotationally scanned optical coherence tomography," J. Opt. Soc. Am. A **23**, 2433–2439 (2006).
8. D. L. Marks, T. S. Ralston, S. A. Boppart, and P. S. Carney, "Inverse scattering for frequency-scanned full-field optical coherence tomography," J. Opt. Soc. Am. A **24**, 1034–1041 (2007).
9. T. S. Ralston, D. L. Marks, P. S. Carney, and S. A. Boppart, "Interferometric synthetic aperture microscopy," Nat. Phys. **3**, 129–134 (2007).
10. J. C. Curlander and R. N. McDonough, *Synthetic Aperture Radar: Systems and Signal Processing* (Wiley-Interscience, 1991).
11. B. Richards and E. Wolf, "Electromagnetic diffraction in optical systems. II. Structure of the image field in an aplanatic system," Proc. R. Soc. London, Ser. A **253**, 358–379 (1959).
12. M. Choma, M. Sarunic, Y. Changhuei, and J. Izatt, "Sensitivity advantage of swept source and Fourier domain optical coherence tomography," Opt. Express **111**, 2183–2189 (2003).

13. R. Leitgeb, C. K. Hitzenberger, and A. F. Fercher, "Performance of Fourier domain vs. time domain optical coherence tomography," Opt. Express **11**, 889–894 (2003).

14. B. J. Davis, T. S. Ralston, D. L. Marks, S. A. Boppart, and P. S. Carney, "Autocorrelation artifacts in optical coherence tomography and interferometric synthetic aperture microscopy," Opt. Lett. **32**, 1441–1443 (2007).

15. Z. Ding, Y. Zhao, H. Ren, J. S. Nelson, and Z. Chen, "Real-time phase-resolved optical coherence tomography and optical Doppler tomography," Opt. Express **10**, 236–245 (2002).

16. P. Hariharan, *Optical Interferometry* (Academic, 2003).

17. D. L. Marks, A. L. Oldenburg, J. J. Reynolds, and S. A. Boppart, "A digital algorithm for dispersion correction in optical coherence tomography," Appl. Opt. **42**, 204–217 (2003).

18. Y. Zhao, Z. Chen, C. Saxer, S. Xiang, J. F. de Boer, and J. S. Nelson, "Phase-resolved optical coherence tomography and optical Doppler tomography for imaging blood flow in human skin with fast scanning speed and high velocity sensitivity," Opt. Lett. **25**, 114–116 (2000).

19. E. Wolf, "Electromagnetic diffraction in optical systems. I. An integral representation of the image field," Proc. R. Soc. London, Ser. A **253**, 349–357 (1959).

20. Y. Feng, R. K. Wang, and J. B. Elder, "Theoretical model of optical coherence tomography for system optimization and characterization," J. Opt. Soc. Am. A **20**, 1792–1803 (2003).

21. H. Weyl, "Expansion of electro magnetic waves on an even conductor," Ann. Phys. **60**, 481–500 (1919).

22. L. Mandel and E. Wolf, *Optical Coherence and Quantum Optics* (Cambridge U. Press, 1996), Chap. 3, pp. 92–146.

23. R. J. Potton, "Reciprocity in optics," Rep. Prog. Phys. **67**, 717–754 (2004).

24. P. C. Hansen, *Rank-Deficient and Discrete Ill-Posed Problems* (SIAM, 1998).

25. M. Born and E. Wolf, *Principles of Optics* (Cambridge U. Press, 1980).

26. H. M. Nussenzveig, *Diffraction Effects in Semiclassical Scattering* (Cambridge U. Press, 1992), Chap. 2.2, pp. 17–20.

27. P. T. Gough and D. W. Hawkins, "Unified framework for modern synthetic aperture imaging algorithms," Int. J. Imaging Syst. Technol. **8**, 343–358 (1997).

28. N. Wiener, *Extrapolation, Interpolation, and Smoothing of Stationary Time Series* (MIT, 1964).

29. M. Mujat, E. Baleine, and A. Dogariu, "Interferometric imaging polarimeter," J. Opt. Soc. Am. A **21**, 2244–2249 (2004).

30. C. Chou, L. C. Peng, Y. H. Chou, Y. H. Tang, C. Y. Han, and C. W. Lyu, "Polarized optical coherence imaging in turbid media by use of a Zeeman laser," Opt. Lett. **25**, 1517–1519 (2000).

31. J. F. de Boer and T. E. Milner, "Review of polarization sensitive optical coherence tomography and Stokes vector determination," J. Biomed. Opt. **7**, 359–371 (2002).